Crystal Plasticity Finite Element Simulation of NiTi Shape Memory Alloy Based on Representative Volume Element

Li Hu[1,2], Shuyong Jiang[1,*], Yanqiu Zhang[1], and Dong Sun[2]

[1]College of Mechanical and Electrical Engineering, Harbin Engineering University, Harbin 150001, China
[2]College of Materials Science and Chemical Engineering, Harbin Engineering University, Harbin 150001, China

Crystal plasticity finite element method based on a representative volume element model, which includes the effect of grain shape and size, is combined with electron backscattered diffraction experiment in order to investigate plastic deformation of NiTi shape memory alloy during uniaxial compression at 400 °C. Simulation results indicate that the constructed representation of the polycrystal microstructure is able to effectively simulate macroscopically global stress-strain response and microscopically inhomogeneous microstructure evolution in the case of various loading directions. According to slip activity and Schmid factor in {110}<100>, {010}<100> and {110}<111> slip modes, <100> slip modes are found to play a dominant role in plastic deformation, while <111> slip mode is found to be a secondary slip mode. In addition, the simulation results are supported well by the experimental ones. With the progression of plastic deformation, the (001) [0$\bar{1}$0] texture component gradually disappears, while the γ-fiber (<111>) texture is increasingly enhanced.

Keywords: shape memory alloys, deformation, crystal plasticity, electron backscattering diffraction, texture

1. INTRODUCTION

NiTi shape memory alloy is widely used in the engineering field because of its shape memory effect. In general, shape memory effect of NiTi shape memory alloy is attributed to phase transformation from B2 austenite to B19' martensite on cooling as well as phase transformation from B19' martensite to B2 austenite on heating [1]. As we know, plastic deformation plays an important role in manufacturing NiTi shape memory alloy products, such as NiTi wire, bar, tube, strip and sheet [2-4]. It is generally accepted that plastic deformation has a significant influence on the microstructures of NiTi shape memory alloy, such as grain size, grain morphology, grain orientation, substructure and so on, which affect further shape memory effect and mechanical properties of NiTi shape memory alloy [5,6]. In particular, depending on temperatures, NiTi shape memory alloy belongs to either B2 austenite or B19' martensite. This means that plastic deformation mechanism of NiTi shape memory alloy is very complicated. It has been reported that in the case of various temperatures, NiTi shape memory alloy exhibits multiple plastic deformation mechanisms, such as stress-induced martensite phase transformation, dislocation slip, deformation twinning, grain boundary slide, grain rotation, dislocation climb and grain boundary migration [1,7].

Therefore, it is of great importance to perform an in-depth investigation into plastic deformation mechanisms of NiTi shape memory alloy for the purpose for controlling its microstructures.

However, it is well known that experimental methods possess a certain limitation in terms of revealing plastic deformation mechanisms of metallic alloy, so numerical method, such as finite element method (FEM), becomes a perfect candidate for clarifying plastic deformation law of metallic alloy [8,9]. However, FEM based on macroscopic phenomenological constitutive theory is unable to meet the requirement for capturing the microstructural evolution of polycrystalline metallic alloy subjected to plastic deformation. As a consequence, crystal plasticity finite element method (CPFEM), which is based on the constitutive model for dislocation slip or deformation twinning, becomes a superior candidate for investigating plastic deformation of polycrystalline metallic alloy in terms of multi-scale methods, including macroscale, mesoscale, and microscale [10-12]. Though CPFEM has been used to investigate the superelastic deformation and transformation-induced plasticity of NiTi shape memory alloy [13-15], few literatures have reported that CPFEM is used for investigating mechanical response, microstructural evolution, texture evolution and inhomogeneous deformation of NiTi shape memory alloy subjected to large plastic strain.
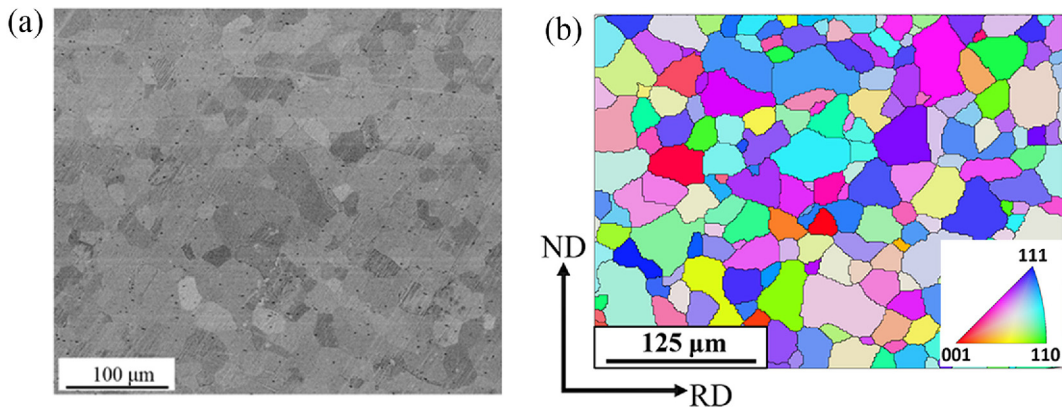
In the present study, plastic deformation of NiTi shape memory alloy during uniaxial compression along the various loading directions at 400 °C is investigated by combining CPFEM

with electron backscattered diffraction (EBSD) experiment. In addition, the representative volume element (RVE) model and constitutive model based on dislocation slip are used in the CPFEM.

2. EXPERIMENTAL PROCEDURE

The NiTi shape memory alloy samples with the diameter of 4 mm and the height of 6 mm were prepared from the as-received NiTi shape memory alloy bar with a nominal composition of $Ni_{50.9}Ti_{49.1}$(at%) by means of electro-discharge machining (EDM). In addition, the as-received NiTi shape memory alloy bar was prepared by virtue of vacuum induction melting method and subsequent rolling at 800 °C. The transformation temperatures of the as-received NiTi shape memory alloy sample are as follows: $M_s = -27.2$ °C, $M_f = -41.7$ °C, $A_s = -17.3$ °C and $A_f = -4.1$ °C. The NiTi shape memory alloy samples were used for uniaxial compression test at the various deformation degrees at the temperature of 400 °C and then were quenched into water at room temperature in order to keep the deformed microstructure. The compressive deformation degrees were determined as 20%, 30%, and 40%, respectively. The compression tests were carried out on INSTRON-5500R universal testing machine at the strain rate of 0.001 s^{-1}. To acquire the evolution of microstructure and texture of NiTi shape memory alloy samples, scanning electron microscope (SEM) experiment and electron backscattered diffraction (EBSD) experiments were conducted on the as-received specimen and these deformed specimens using a Zeiss Supra 55 SEM coupled with OXFORD EBSD instrument. Due to the relatively large scanning area, the scan step in EBSD experiment was chosen to be 2 μm in comprehensive consideration of scanning time and scanning resolution. Figure 1 shows the initial microstructure via SEM and EBSD experiments. It is obvious that the initial microstructure is composed of equiaxed grains and the average grain size is finally determined to be about 25 μm.

3. CRYSTAL PLASTICITY FINITE ELEMENT MODEL

3.1. Crystal plasticity constitutive model

In our previous work, deformation twinning was not observed in the $Ni_{50.9}Ti_{49.1}$ (at%) shape memory alloy sample subjected to compression deformation at 400 °C [7]. Furthermore, it can be generally accepted that 400 °C is higher than the temperature of M_d, above which stress-induced martensite phase transformation does not take place. Therefore, in the present study, dislocation slip instead of deformation twinning plays a dominant role in plastic deformation of NiTi shape memory alloy at 400 °C. As a consequence, {110}<100>, {010}<100> and {110}<111> slip modes are introduced into crystal plasticity constitutive model of NiTi shape memory alloy in order to accommodate all the strains for generalized polycrystalline plasticity [1].

In the framework of crystal plasticity [16], the total deformation gradient is decomposed into the elastic and plastic components through a multiplicative decomposition:

$$\mathbf{F} = \mathbf{F}^*\mathbf{F}^P \tag{1}$$

where $\mathbf{F}^P$ stands for the crystalline slip on specific slip plane and along specific slip direction and $\mathbf{F}^*$ represents the elastic stretching and rigid-body rotation, respectively.

The velocity gradient $\mathbf{L}$ can be expressed as:

$$\mathbf{L} = \dot{\mathbf{F}}\mathbf{F}^{-1} = \dot{\mathbf{F}}^*\mathbf{F}^{*-1} + \mathbf{F}^*\dot{\mathbf{F}}^P\mathbf{F}^{P-1}\mathbf{F}^{*-1} = \mathbf{F}^*\mathbf{F}^{*-1} + \mathbf{F}^*\mathbf{L}^P\mathbf{F}^{*-1} \tag{2}$$

where $\mathbf{L}^P = \dot{\mathbf{F}}^P\mathbf{F}^{P-1}$ stands for the plastic velocity gradient in intermediate configuration. From the kinematics of dislocation, this term is related to the slipping rate $\dot{\gamma}^\alpha$ of α slip system by the following equation:

$$\mathbf{L}^P = \dot{\mathbf{F}}^P\mathbf{F}^{P-1} = \sum_\alpha \dot{\gamma}^\alpha \mathbf{m}_0^\alpha \otimes \mathbf{n}_0^\alpha \tag{3}$$

where $\mathbf{m}_0^\alpha$ and $\mathbf{n}_0^\alpha$ are the unit vectors which stand for the slip

Fig. 1. Initial microstructure of as-received polycrystalline NiTi shape memory alloy; (a) SEM image and (b) EBSD scan area in rolling-normal (RD-ND) plane.

direction and the normal to the slip plane in the intermediate configuration, respectively, and $\otimes$ stands for the dyadic product of two vectors. It is convenient to translate vectors $\mathbf{m}_0^\alpha$ and $\mathbf{n}_0^\alpha$ in intermediate configuration into corresponding vectors $\mathbf{m}^\alpha$ and $\mathbf{n}^\alpha$ in current configuration according to the following equation.

$$\mathbf{m}^\alpha = \mathbf{F}^* \mathbf{m}_0^\alpha, \mathbf{n}^\alpha = \mathbf{n}_0^\alpha \mathbf{F}^{*-1} \tag{4}$$

Furthermore, the velocity gradient $\mathbf{L}$ can be additive decomposition as the sum of a symmetric deformation tensor $\mathbf{D} = \frac{1}{2}(\mathbf{L} + \mathbf{L}^T)$ and an anti-symmetric rotation tensor $\Omega = \frac{1}{2}(\mathbf{L} - \mathbf{L}^T)$, namely

$$\mathbf{L} = \mathbf{D} + \Omega; \mathbf{D} = \mathbf{D}^* + \mathbf{D}^p; \Omega = \Omega^* + \Omega^p \tag{5}$$

where $\mathbf{D}$ and Ω can be further decomposed into elastic part ($\mathbf{D}^*$, Ω^*) and plastic part ($\mathbf{D}^p$, Ω^p), respectively.

In the framework of rate-dependent single crystal plasticity, the elastic constitutive equation is specified by [17]:

$$\overset{\triangledown}{\sigma}^* + \sigma(\mathbf{I} : \mathbf{D}^*) = \mathbf{L} : \mathbf{D}^* \tag{6}$$

where $\mathbf{I}$ is the second order identity tensor, $\mathbf{L}$ is the tensor of elastic moduli having the full set of symmetries $\mathbf{L}_{ijkl} = \mathbf{L}_{jikl} = \mathbf{L}_{ijlk} = \mathbf{L}_{klik}$. The Jaumann rate $\overset{\triangledown}{\sigma}^*$ is the corotational stress rate on the axes that rotate with the crystal lattice, and it is related to the corotational stress rate on the axes that rotate with the material $\overset{\triangledown}{\sigma}$ by the following equation.

$$\overset{\triangledown}{\sigma}^* = \overset{\triangledown}{\sigma} + \Omega^p \cdot \sigma - \sigma \cdot \Omega^p \tag{7}$$

where $\overset{\triangledown}{\sigma} = \dot{\sigma} - \Omega \cdot \sigma + \sigma \cdot \Omega$.

Based on the Schmid law, the slipping shear rate $\dot{\gamma}^\alpha$ on individual slip systems can be determined by a simple rate-dependent power law relation [18].

$$\dot{\gamma}^\alpha = \dot{\gamma}_0 |\tau^\alpha/g^\alpha|^n \operatorname{sign}(\tau^\alpha/g^\alpha) \tag{8}$$

where, n stands for the rate dependency and if the material is highly rate-dependent, a typical value of 10 can be used, and if the material is rate independent, a large value can be chosen up to 50 [19]. In the present study, the value of n is chosen to be 20, which indicates that NiTi shape memory alloy possesses a certain rate-dependency at medium to high temperatures as reported in reference [20]. $\dot{\gamma}_0$ is a reference shear strain rate and it is chosen to be $0.001s^{-1}$ in consideration of quasi-static loading rate. τ^α and g^α are the resolved shear stress on the slip system α and the slip resistance of this system, respectively. Furthermore, the increase rate of g^α is given as follows.

$$\dot{g}^\alpha = \sum_\beta^N h_{\alpha\beta} \dot{\gamma}^\beta \tag{9}$$

where $h_{\alpha\beta}$ is the slip hardening modulus, and the sum operation is performed over all activated slip systems. $h_{\alpha\alpha}$ is known as self-hardening modulus and it is derived from the hardening of slip system itself. In addition, $h_{\alpha\beta}$ ($\alpha \neq \beta$) is called latent-hardening modulus which indicates that the hardening is caused by another slip system.

A simple form is used for hardening model [21].

$$h_{\alpha\alpha} = h(\gamma) = h_0 \operatorname{sech}^2 \left| \frac{h_0 \gamma}{\tau_s - \tau_0} \right|, \gamma = \sum_\alpha \int_0^t |\dot{\gamma}^\alpha| dt$$
$$h_{\alpha\beta} = q h(\gamma) \ (\alpha \neq \beta) \tag{10}$$

where h_0 is the initial hardening modulus, τ_0 is the initial yield stress, τ_s is the saturation stress, γ is the total shear strain in all slip systems, and q is the ratio of latent hardening to self hardening behavior of crystalline and $q = 1.4$ is used in the present study [1]. The numerical implementation of the aforementioned crystallographic formulations is specifically explained in the reference [22] and the code of crystal plasticity model, based on the work of Huang [17], is embedded as a user-supplied subroutine UMAT in the finite element software ABAQUS, where the implicit integration algorithm is adopted.

3.2. Establishment of polycrystalline aggregate model

The effective properties of crystal plasticity for polycrystalline NiTi shape memory alloy are determined by means of the finite element simulation of representative volume element (RVE) model which reflects the characteristics of microstructure. At present, there are mainly two different types of RVE models [23]. One kind of RVE model, where only one element stands for one grain, deals with a simple computation model and thus corresponds to a voxel approach. The other RVE model, where each crystal is discretized with many cubic finite elements, represents a relatively sophisticated computation model and thus corresponds to a realistic polycrystalline microstructure. Though these voxel RVE models are based on rather simplified geometrical representations, they can provide very good results, which are in good agreement with texture measurement and mechanical properties with high accuracy and computational efficiency [24]. When one is interested in understanding the inter-granular and intra-granular behavior in microscale, these realistic RVE models with refined mesh are used because the accurate representation of grain shape and especially grain boundary surface is important in capturing the heterogeneous deformation in polycrystal [25,26]. In the present study, those two kinds of different representation of microstructure are used, as shown in Fig. 2. A voxel model with 1000 grains is made up by a regular mesh of 10×10×10 cubic finite elements. This model is used in the course of parameter determination because of low computational cost and high accuracy in predicting the stress-strain response and the texture evolution of metal materials [27]. The boundary conditions applied in the course of parameter determination
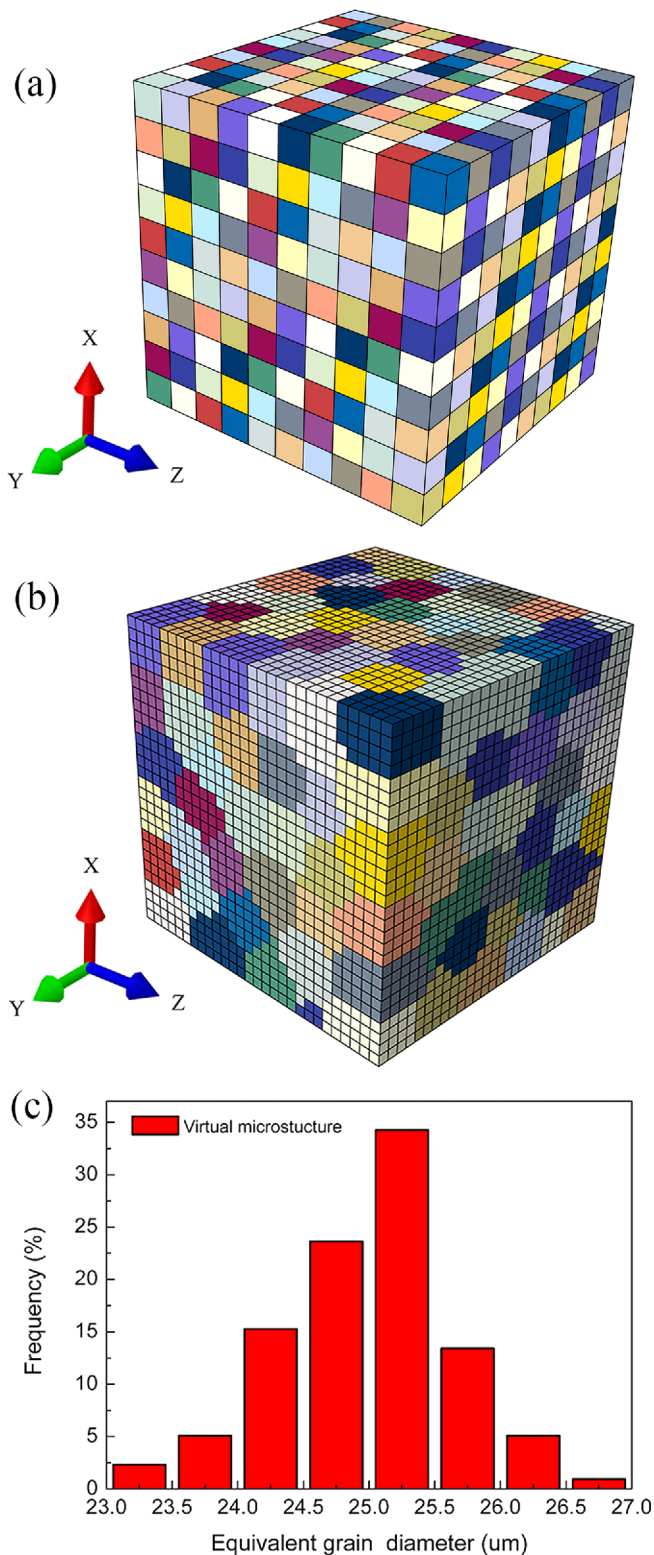
Fig. 2. RVE model of polycrystalline NiTi shape memory alloy; (a) Voxel model with 1000 cubic finite elements in which each element represents a single crystal, (b) Realistic RVE model containing 216 grains discretized with 21952 cubic finite elements, and (c) The statistical analysis of equivalent grain diameter in individual grains of the realisitc RVE model.

are realized by means of periodic boundary conditions (PBCs) in x, y and z directions of the voxel RVE model which would be compressed in x direction at the strain rate of 0.001 s⁻¹. A realistic RVE model containing 216 grains is depicted in Fig. 2(b) and it is constructed by means of a free open source software package NEPER [28]. Moreover, its microstructure is based on the SEM and EBSD experiments performed on the as-received specimen of NiTi shape memory alloy. Figure 2(c) shows the distribution of grain size in the constructed realistic RVE model and the average grain size is determined to be about 25 μm, which is similar to the experimental result. Unlike the applied PBCs in the voxel model, these boundary conditions used in the realistic model are based on the fact that all faces are constrained to remain planar and an uniaxial compression deformation in x, y or z directions is applied respectively at a total deformation degree of 40% at the strain rate of 0.001 s⁻¹. Compared to the PBCs, this boundary conditions are easy to establish and it has been confirmed that there are no big differences in the results of stress-strain curve and texture evolution anyway [26,29].

In the present study, the initial orientations of individual grains in either RVE model of the polycrystal are extracted from the EBSD data by discretizing the orientation distribution function (ODF). Figure 3 shows a comparison between the measured texture from the initial microstructure and the corresponding simulated texture with 216 grains. It can be seen that the synthetic pole figures reproduce the main features of the experimental ones although the limited number of crystals in the model (particularly for 216 grains) influences the maximum and minimum intensities.

3.3. Parameter calibration

The anisotropic elastic tensor for single crystal NiTi shape memory alloy can be specified in terms of three stiffness param-
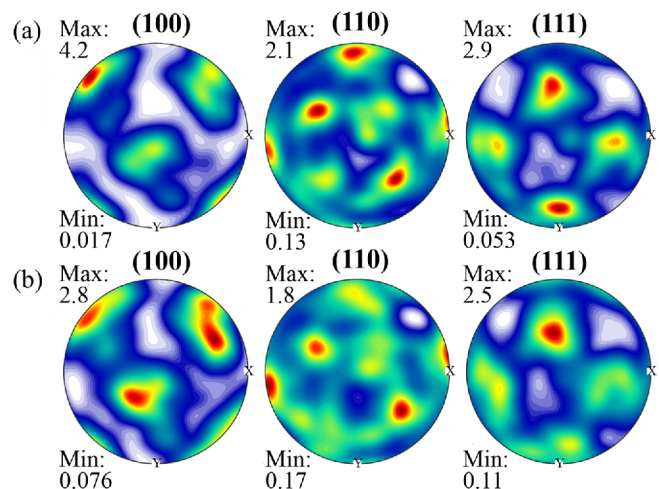
Fig. 3. Pole figures for texture in the initial state; (a) Measured results by means of EBSD experiment and (b) Simulated ones on the basis of 216 extracted grain orientations by discretizing ODF.

Table 1. Material parameters of as-received NiTi shape memory alloy

C_{11}	C_{12}	C_{44}	h_0	τ_s	τ_0	$\dot{\gamma}_0$	q	n
130 GPa	98 GPa	34 GPa	1484.0 MPa	364.5 MPa	186.5 MPa	0.001 s^{-1}	1.4	20

eters, namely C_{11}, C_{12} and C_{44}. Values of these elastic parameters are determined as $C_{11} = 130$ GPa, $C_{12} = 98$ GPa and $C_{44} = 34$ GPa [13]. Based on the constructed voxel model with 1000 grains as well as the correspondingly extracted orientations from ODF measured by EBSD experiment, the material parameters used in the single-crystal constitutive model are determined by back-fitting the mechanical result in the voxel model to the mechanical response in the uniaxial compression experiment. Since Lee *et al.* [30] has reported that in the case of crystal plasticity finite element simulation, the global mechanical behavior is sensitive to the adopted material parameters, so systematic variations of material parameters are important in the procedure of parameter identification. In terms of varying the parameters, a "trial-error" procedure is used in the present study to optimize the numerical results by means of observing the difference between the numerical stress-strain curve and the experimental one. In general, "trial-error" procedure is time consuming, but its results with respect to parameter identification are not as "improper" as the term might indicate [26]. Finally, in this way, a set of best-fit constitutive parameters is determined and the adopted parameters are shown in Table 1.

4. RESULTS AND DISCUSSION

4.1. Effect of loading directions on local microstructure response

Based on the realistic RVE model containing 216 grains, the effect of loading direction is examined by comparing the simulation results for uniaxial compression in the in x , y and z directions. Figure 4 shows the contour plots of the maximum principal strain and the second Euler angle (in radians) under the various loading directions.

As is expected, the response of individual grain to various loading directions depends on the crystallography of each grain. It can be seen from Figs. 4(a), 4(c), and 4(e) that in the case of various loading conditions, strain is heterogeneously distributed within the polycrystalline aggregation. It seems that strain concentration always appears near the grain boundaries and on the surfaces of adopted RVE model. It can be noted that under three various loading conditions, material parameters, initial texture and grain morphology are definitely identical, so the divergence of strain distribution is attributed to the difference in the rotation of grains for the purpose of accommodating plastic deformation of individual grains. This aspect can be confirmed by the diverse distributions of second Euler angle in Figs. 4(b), 4(d), and 4(f). Furthermore, in the case of uniaxial compression in different loading directions,

the local orientation varies from the grain boundary to the grain interior, which is responsible for the texture evolution and heterogeneous strain distribution of NiTi shape memory alloy. It can be concluded that the loading direction has an influence on the local material response in the individual grains.

In order to correlate the simulated material response to a variety of loading directions, the simulation results from the realistic RVE model are now analyzed. The scale quantity of von Mises stress, which represents the intensity of the three-dimensional stress state, proves valuable in deriving information from the complex three-dimensional stress state at a material point. Figure 5 shows the spatial variation of the von Mises stress resulting from an applied deformation degree of 40% in the x, y, and z directions, where only those areas in which the value of von Mises stress exceeds 1000 MPa are highlighted. As is expected, local stress state represented by von Mises stress is found to be heterogeneous in the RVE model. Therefore, these results have an emphasis on the effect of applied loading directions on the local material response. Another interesting result in Fig. 5 is that some areas with maximum stress are found to be located on the free surfaces. This is probably caused by the constraints of the adopted boundary conditions. Finally, it can be noted from Fig. 5 that even in the case of a simple uniaxial applied load, local stress response is also pretty complex. As a result, CPFEM based on a realistic RVE model is of great importance in understanding the heterogeneously local stress response.

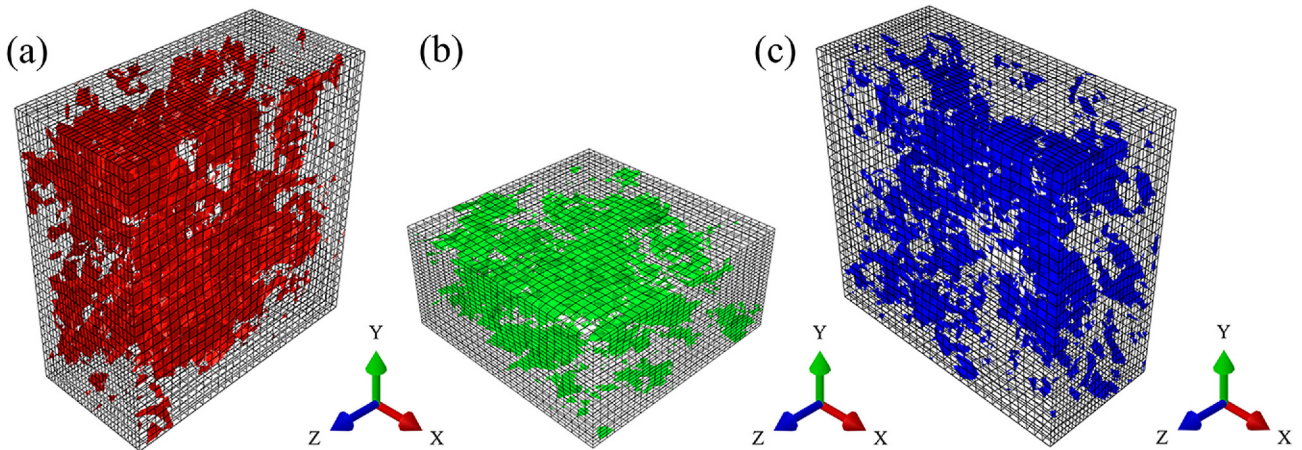### 4.2. Effect of loading directions on global mechanical response

To obtain the global response of material, homogenization based on averaging theorem over the realistic RVE model is adopted to make the transition from micro- to macro-variables of the RVE model. The global stress-strain curves along the various loading axes are demonstrated in Fig. 6. It is worth mentioning that the material parameters used in the present study are calibrated by fitting the simulated response of voxel RVE model with 1000 grains to the experimental data by means of 'trial-error' method. By comparison with the experimental results, the simulated results of finite element models corresponding to 216 grains are able to capture the main characteristics of material response. On the one hand, the simulated results verify that the deformation behavior of NiTi shape memory alloy experiences an initial elastic deformation stage and a subsequent plastic deformation stage. Moreover, with the increase in plastic strain, NiTi shape memory alloy exhibits a continuously and monotonously declining hardening rate. On the other hand, the simulated material behavior shows a relatively soft response, where the flow stress is 4.51 MPa,
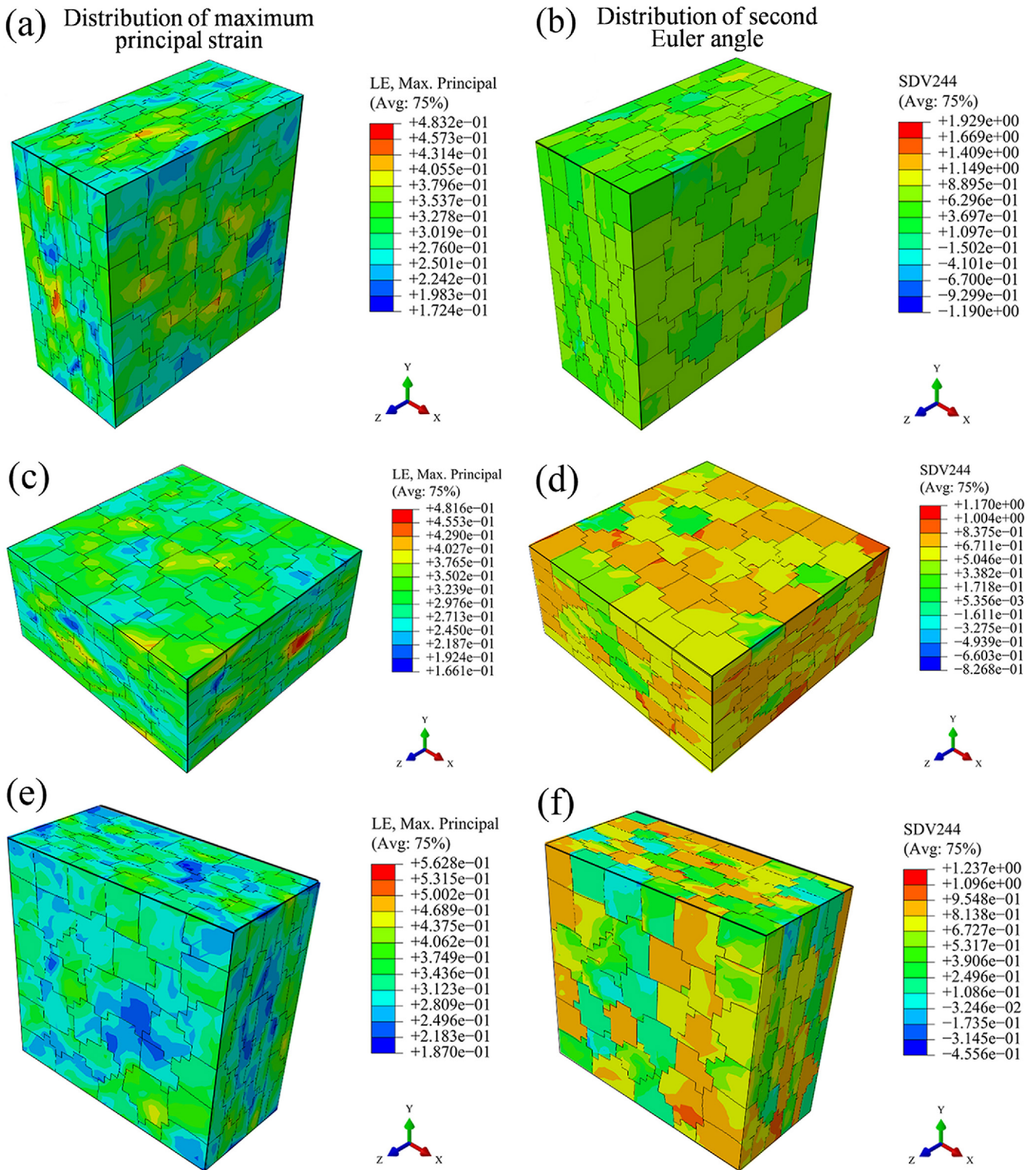
Fig. 4. Contour plots of maximum principal strain and the second Euler angle of adopted RVE model subjected to uniaxial compression along various loading directions; (a, b) X direction, (c, d) Y direction, and (e, f) Z direction.

15.10 MPa and 13.67 MPa, respectively lower than the measured stress at the deformation degree of 40%. The difference between the simulated results and the experimental ones should be attributed to the fact that the realistic RVE model can accommodate heterogeneous plastic deformation between neighboring grains, which results in a relatively soft flow

Fig. 5. Effect of loading directions on the distribution of von Mises stress in adopted RVE model at a deformation degree of 40%, where the areas in which the resulting stress exceeds 1000 MPa are shown in color; (a) Loading in x direction, (b) Loading in y direction, and (c) Loading in z direction.
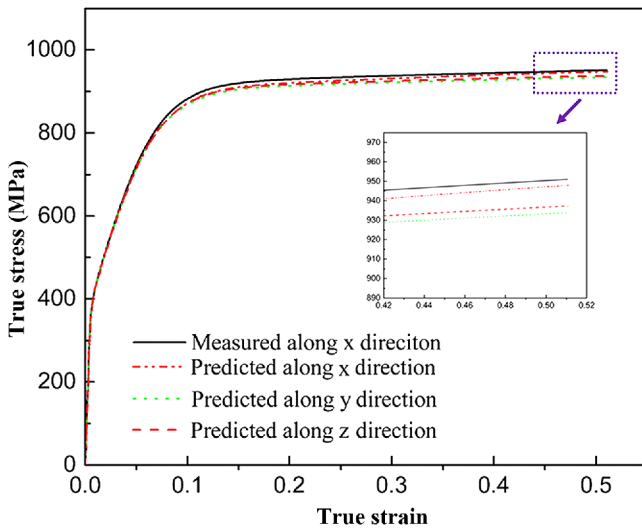
Fig. 6. Experimental stress-strain curve under the condition of uniaxial compression and numerical results by performing finite element simulations on the realistic RVE model of 216 grains subjected to uniaxial compression in x, y and z directions, respectively.

response, whereas the voxel model used for fitting material parameters provides a harder flow response because the deformation is over-constrained to maintain the compatibility between adjacent grains [27]. In addition, the global stress-strain response in the y and z loading directions exhibits a certain similarity, as shown in Fig. 6. The phenomenon indicates that the RVE model shows some manner of material symmetry in y-z plane.

4.3. Texture evolution of NiTi shape memory alloy during uniaxial compression

According to the aforementioned results, it can be noted that the simulated stress-strain response is in better agreement with the experimental one in the case of loading in x direction.

Therefore, the texture evolution of NiTi shape memory alloy samples at the deformation degrees of 20%, 30%, and 40% is obtained by means of EBSD experiment, and then the experimental result is compared with the predicted texture obtained from CPFEM simulation in the case of loading in x direction, as shown in Fig. 7. These inverse pole figures are derived from the lattice plane of which the normals are parallel to the loading direction. It can be observed from Fig. 7 that the simulated result is in good agreement with the experimental one. The phenomenon indicates that CPFEM based on the realistic RVE model is able to accurately capture the texture evolution of NiTi shape memory alloy under uniaxial compression deformation. Furthermore, with the increase in the plastic strain, the pole intensity of {111} gradually increases, while the pole intensity of {110} decreases continuously. This phenomenon indicates that in the case of uniaxial compression, a crystallographic plane gradually rotates to be vertical to the loading direction, which contributes to the formation of the <111> fiber texture.

To further verify the texture evolution predicted by CPFEM based on the realistic RVE model, ODF for section of $\varphi_2 = 45°$ in Euler space for NiTi shape memory alloy subjected to the uniaxial compression at the various deformation degrees, including 20%, 30%, and 40%, is illustrated in Fig. 8, and the corresponding ODF is in contrast with the main ideal orientations. It can be generally accepted that ODF plays a significant role in clarifying the texture components during texture evolution. By comparison with the ideal ODF section, it can be seen in Fig. 8(b) that when NiTi shape memory alloy sample is compressed at the deformation degree of 20%, the dominant textures are composed of $(001)[0\bar{1}0]$ texture component and γ-fiber (<111>) texture component, where the <111> axis is parallel to the loading direction. With the progression of plastic deformation, the $(001)[0\bar{1}0]$ texture component gradually disappears, while the γ-fiber (<111>) texture is increas-
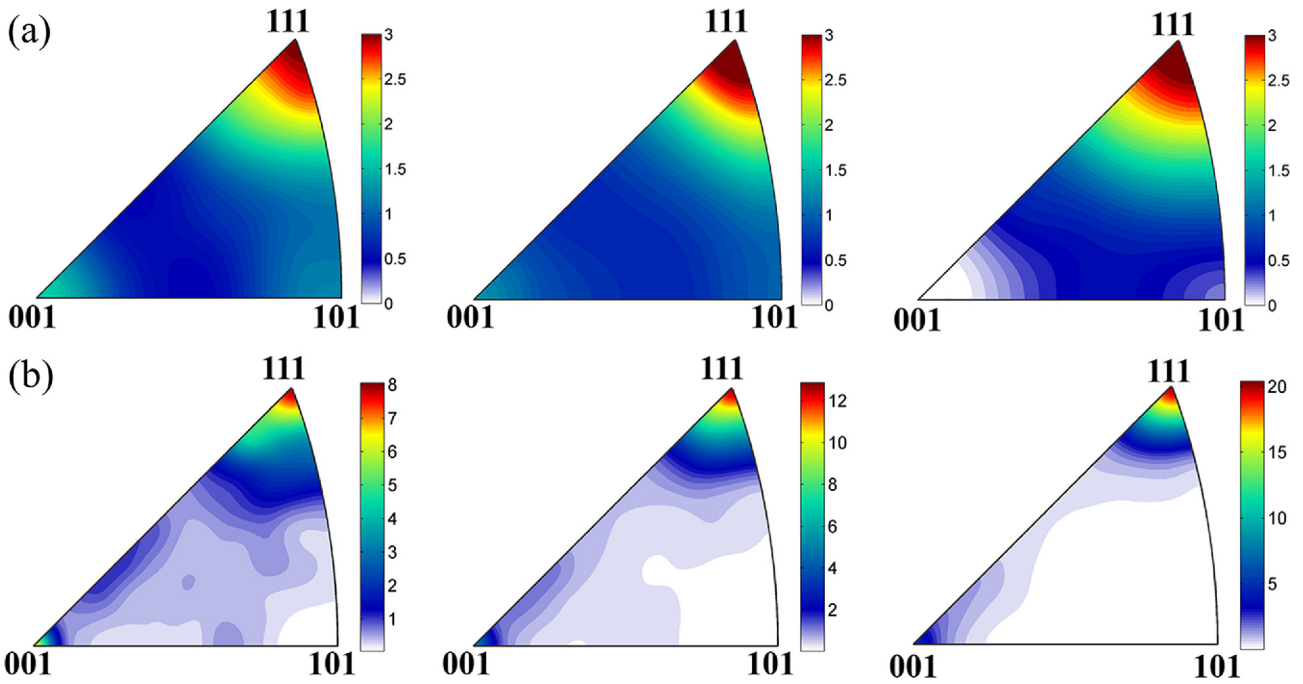
Fig. 7. Inverse pole figures showing comparisons between (a) measured and (b) simulated texture evolution at the deformation degrees of 20%, 30%, and 40%, respectively.
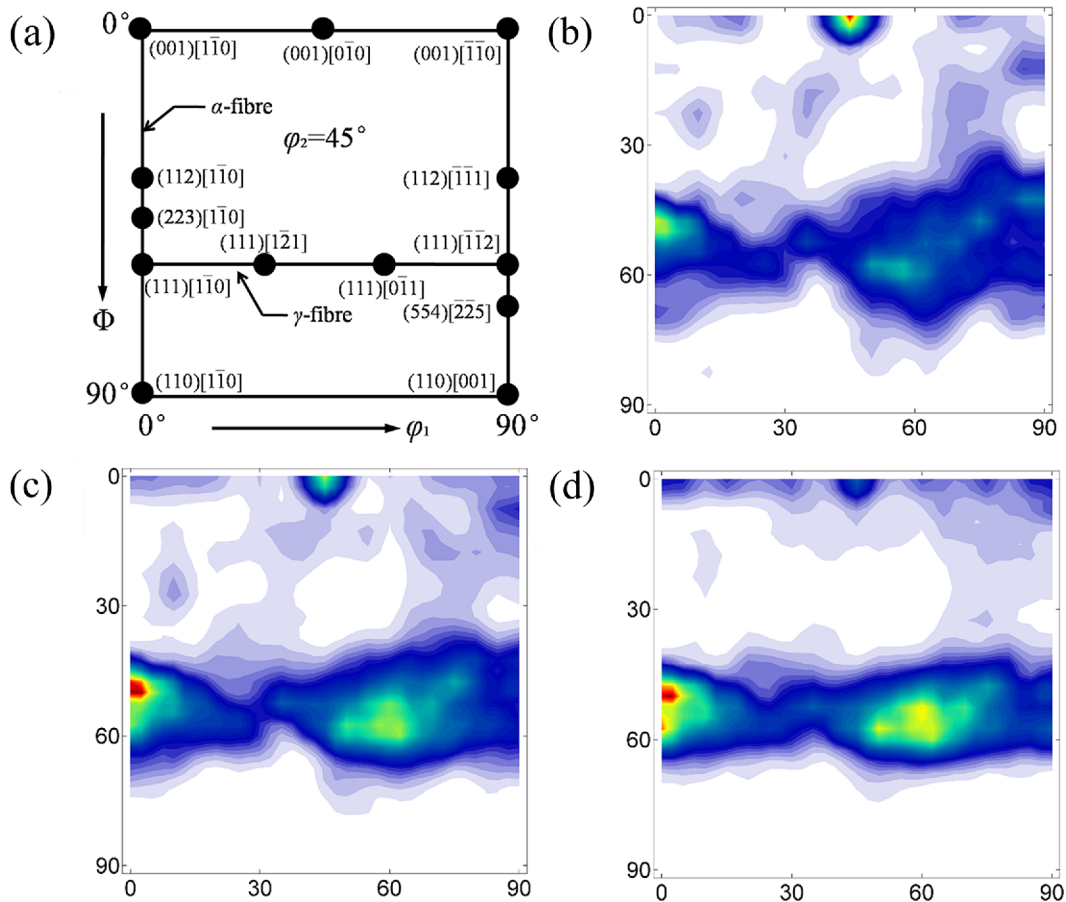

Fig. 8. ODF for section of $\varphi_2 = 45°$ determined by (a) ideal orientations and ODF for section of $\varphi_2 = 45°$ in Euler space for the realistic RVE model of NiTi shape memory alloy subjected to the compression deformation degrees of (b) 20%, (c) 30%, and (d) 40%.

ingly enhanced. This phenomenon is consistent with the observation in Fig. 7.

4.4. Contribution of slip activity to plastic deformation of NiTi shape memory alloy

According to the aforementioned results, it can be noted that CPFEM is able to effectively predict the stress-strain response and the texture evolution of NiTi shape memory alloy during uniaxial compression. In the present study, crystal plasticity constitutive model is established on the basis of dislocation slip. Therefore, it is necessary to clarify the contribution of slip activity to plastic deformation. In order to analyze the slip activity during plastic deformation, the methodology reported by Knezevic *et al.* [31] has been adopted in the present study, where a measurement of the relative contribution to shear per slip mode α normalized by the total contribution of all slip systems is given by the following expression.

$$Activity^{\alpha} = \frac{\sum_{1}^{N_s} \dot{\gamma}^s}{\frac{1}{N_\alpha N_s} \sum_{1}^{N_\alpha} \sum_{1}^{N_s} \dot{\gamma}^s} \tag{21}$$

where N_α and N_s are the total number of slip modes and the total number slip systems per slip mode, respectively, and $\dot{\gamma}^s$ is the shear rate on individual slip system.

The slip activity of each slip mode is captured in the case of uniaxial compression in x direction at the strain rate of 0.001 s^{-1}, as shown in Fig. 9. It can be seen from Fig. 9 that the slip activity of {110}<100> slip mode increases with the increase
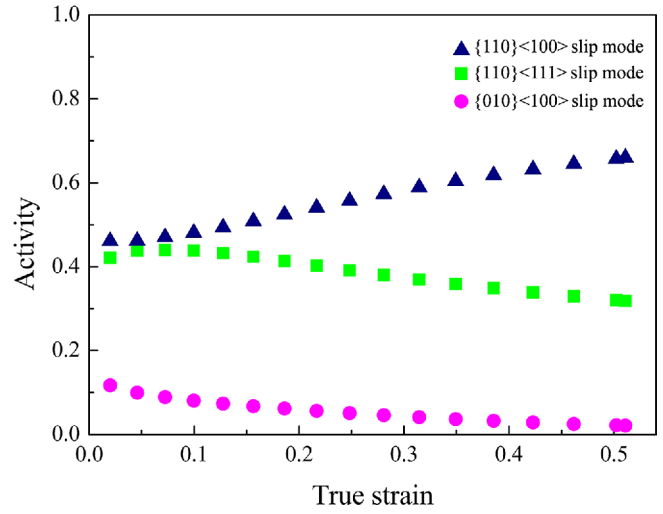
Fig. 9. Predicted relative slip activities of slip modes for uniaxial compression of NiTi shape memory alloy along x direction.
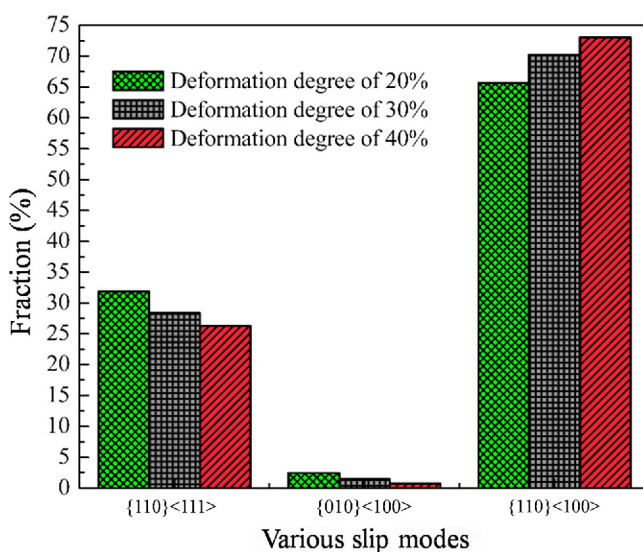
in plastic strain, while the slip activity of {110}<111> and {010}<100> slip modes decreases with the increase in plastic strain. In particular, {110}<111> and {110}<100> slip modes have similar slip activities at the initial stage of deformation, but the difference becomes more and more apparent with the increase of plastic strain. However, {010}<100> slip mode possesses the relatively smaller slip activity at the initial stage of deformation and its contribution to plastic deformation continuously reduces with the increase of plastic strain. These results indicate that the contribution of {110}<100> slip mode
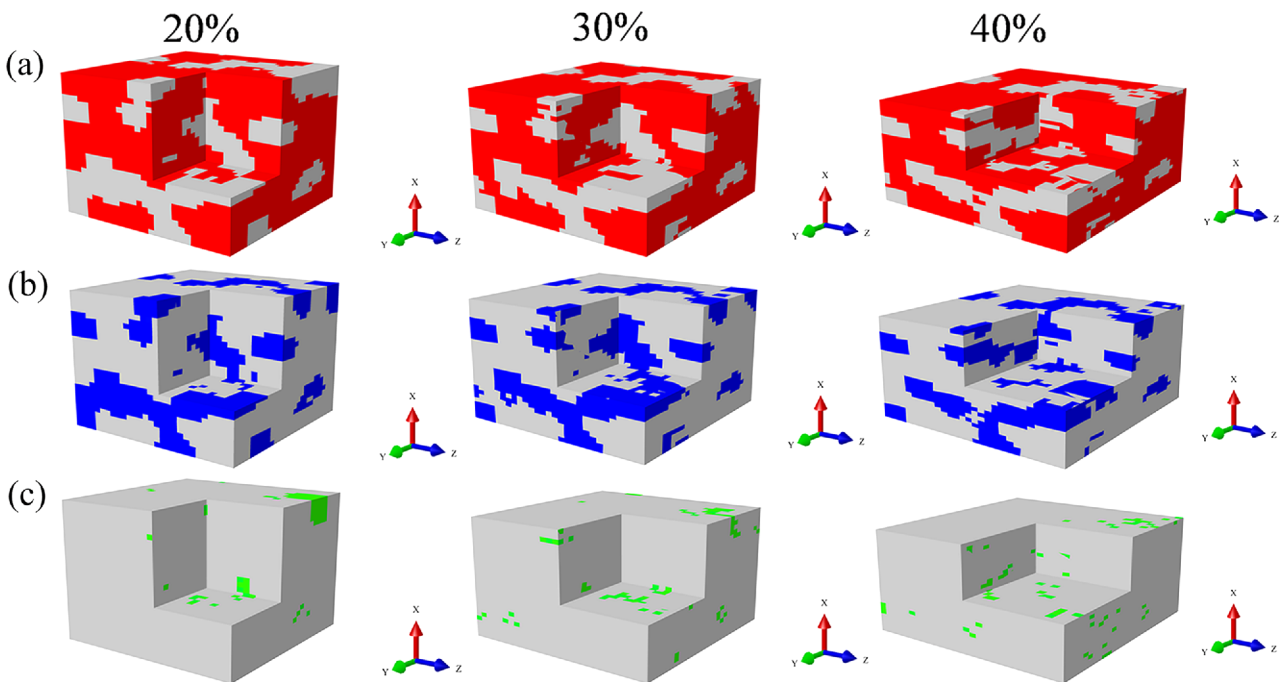
Fig. 10. Spatial distribution of maximum Schmid factor with respect to various slip modes at the various deformation degrees; (a) {110}<100> slip mode, (b) {110}<111> slip mode, and (c) {010}<100> slip mode.

to plastic strain is dominant in plastic deformation of NiTi shape memory alloy.

It is well known that Schmid factor plays a significant role in understanding plastic deformation based on dislocation slip. It is generally accepted that in the case of a given external stress, the larger Schmid factor contributes more to plastic deformation by means of dislocation slip. Therefore, to further give an insight into the contribution of slip activity to plastic deformation, the Schmid factor of individual slip system with respect to the loading direction is calculated in each integration point and consequently the spatial distribution of the maximum Schmid factor with respect to various slip modes is determined at the deformation degrees of 20%, 30%, and 40%, respectively, as shown in Fig. 10. It can be seen from Fig. 10 that with the progression of plastic deformation, in the case of all the three slip modes, the maximum Schmid factor exhibits a heterogeneously spatial distribution. Furthermore, in the case of the {110}<100> slip mode, the spatial distribution areas of the maximum Schmid factor increase with the increase in plastic strain, whereas in the case of {110}<111> and {010} <100> slip modes, the spatial distribution areas of the maximum Schmid factor decrease with the increase in plastic strain. In addition, statistical analysis for the spatial distribution of the maximum Schmid factor with respect to the various slip modes is obtained in the case of the various deformation degrees, as shown in Fig. 11. It can be noted that in the case of all the deformation degrees including 20%, 30%, and 40%, {110}<100> slip mode takes up the largest fraction according to the number of the largest Schmid factor which it possesses, while {010}<100> slip mode takes up the smallest fraction according to the number of the largest Schmid factor which it possesses. In addition, with the increase of the defor-

mation degree, the fraction of the largest Schmid factor which {110} <111> and {010}<100> slip modes possess gradually decreases, while the fraction of the largest Schmid factor which {110} <100> slip mode possesses gradually increases. These results demonstrate a similar trend with the aforementioned ones with respect to the contribution of slip activity in the plastic deformation. Consequently, these results in terms of Schmid factor provide an indirect support for the contribution of individual slip mode to the plastic deformation, where {110}<100> slip mode contributes most to plastic deformation, then the {110} <111> slip mode, finally the {010}<100> slip mode. It can be concluded that <100> slip modes play a dominant role in plastic deformation of NiTi shape memory alloy, whereas the <111> slip mode is a secondary slip mode.

4.5. Inhomogeneous deformation of NiTi shape memory alloy during uniaxial compression

With the progression of plastic deformation, since there exist differences in terms of grain orientation and grain morphology within the polycrystalline NiTi shape memory alloy, dislocation slip in the individual grains exhibits a certain discrepancy, which leads to the variation of local orientation from the grain boundary to the grain interior, as shown in Fig. 12. The misorientation between the orientation in each individual scanning point and the mean orientation in the corresponding individual grains is also illustrated in Fig. 12. It can be found from Fig. 12 that in the case of all different deformation degrees, misorientation is heterogeneously distributed in each scanning area. In addition, according to the statistical analysis with respect to misorientation, it can be seen that the misorientation less than 15° is dominant in NiTi shape memory alloy subjected to plastic deformation. The heterogeneous distribution of misorientation lays the foundations for understanding the inhomogeneous strain distribution of NiTi shape memory alloy subjected to uniaxial compression at the grain level.

To further characterize and verify the heterogeneity of plastic deformation in the polycrystalline NiTi shape memory alloy, based on the method reported by Wert *et al.* [32], the lattice rotation angles are calculated and visualized by means of CPFEM simulation. The lattice rotation angle represents the angle by which slip system needs to rotate before deformation and after deformation. In general, the lattice rotation angle has three components, including the angles around the x, y and z axes, respectively. According to Figs. 13(a)-(c), it can be seen that the rotation angles along three specific axes are heterogeneously distributed in the microstructure, which is responsible for heterogeneous deformation among the grains and in the grain interior, as shown in Fig. 13(d). As a consequence, the inhomogeneous distribution of the rotation angle plays a significant role in the inhomogeneous deformation of polycrystalline NiTi shape memory alloy in terms of grain scale.
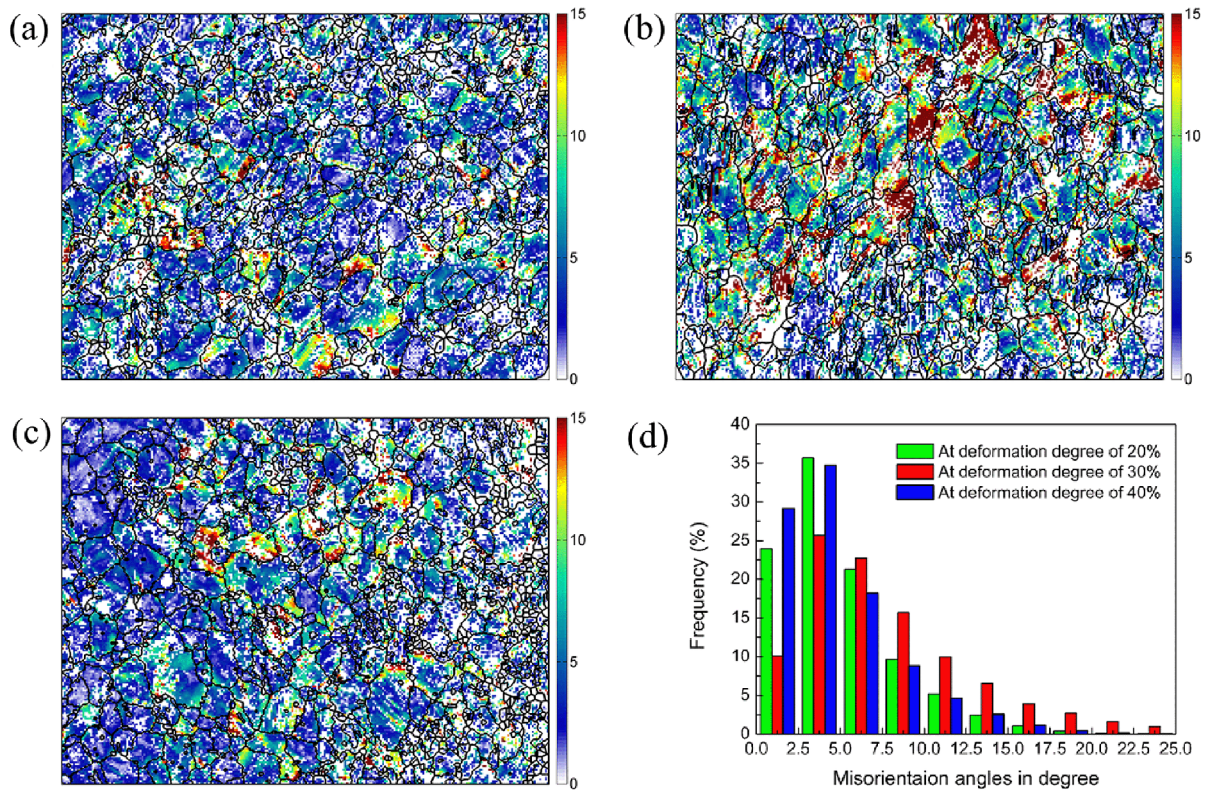

Fig. 11. Statistical analysis for spatial distribution of maximum Schmid factor with respect to various slip modes in the case of the various deformation degrees.

Fig. 12. Microstructure evolution and misorientation distribution of NiTi shape memory alloy subjected to uniaxial compression at the deformation degrees of (a) 20%, (b) 30%, and (c) 40%, and (d) Statistical analysis of misorientation corresponding to the aforementioned deformation degrees.
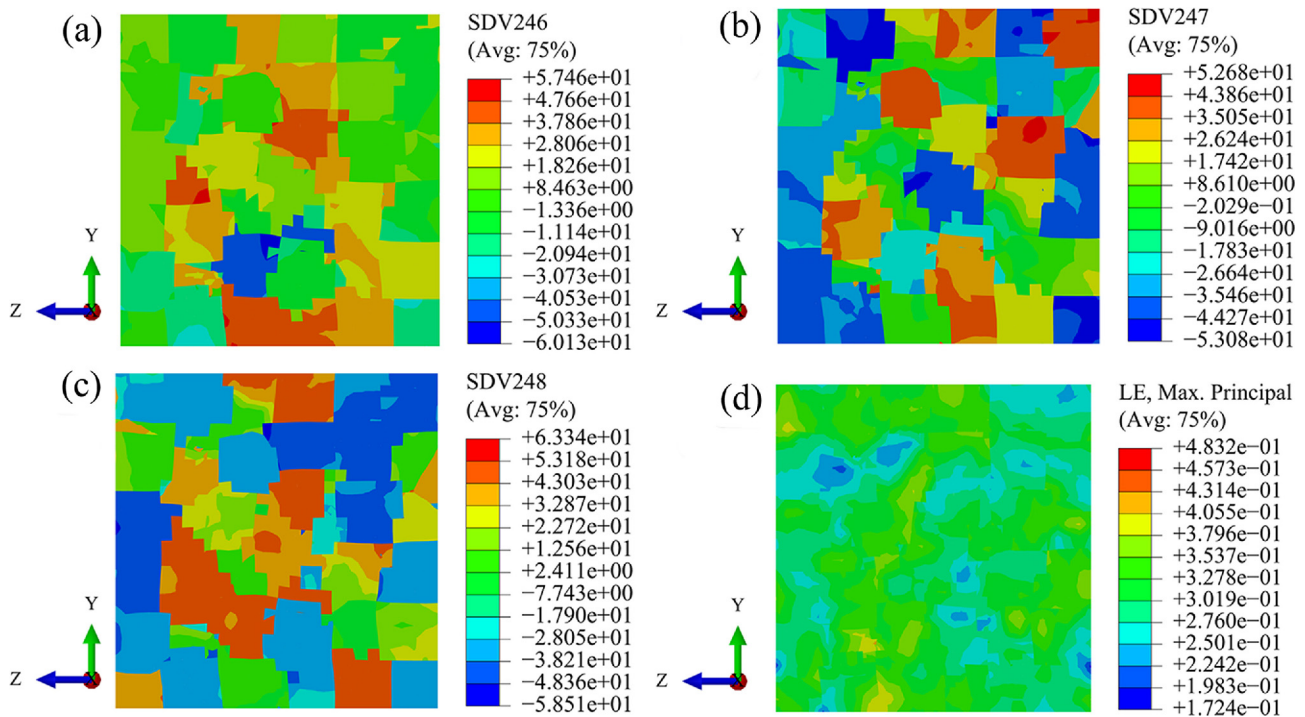
Fig. 13. Distribution of rotation angles and the corresponding strain at the deformation degree of 40% in the middle cross section of the microstructure along x direction; (a) Rotation angle around x([100]) direction, (b) Rotation angle around y([010]) direction, (c) Rotation angle around z([001]) direction, and (d) The corresponding strain distribution.

5. CONCLUSION

Crystal plasticity finite element method (CPFEM) based on the realistic representative volume element (RVE) model is combined with electron backscattered diffraction (EBSD) experiment in order to investigate plastic deformation of NiTi shape memory alloy during uniaxial compression at 400 °C, the following conclusions can be drawn.

(1) Loading direction has an impact on the microscale and macroscale response of crystal plasticity finite element model of NiTi shape memory alloy. Moreover, the CPFEM based on the realistic RVE has the capability to simulate the complicated and heterogeneous local material response in microstructure.

(2) According to slip activity and Schmid factor, the contribution of {110}<100>, {010}<100> and {110}<111> slip modes to the plastic deformation of NiTi shape memory alloy is investigated based on CPFEM simulation. It can be concluded that <100> slip modes play a dominant role in plastic deformation of NiTi shape memory alloy, while the <111> slip mode is a secondary slip mode.

(3) CPFEM based on the realistic RVE is able to effectively simulate texture evolution of NiTi shape memory alloy subjected to uniaxial compression. The simulation results are consistent with the experimental ones. With the progression of plastic deformation, the (001)[0$\bar{1}$0] texture component gradually disappears, while the γ-fiber (<111>) texture is increasingly enhanced.

(4) The inhomogeneous plastic deformation of polycrystalline NiTi shape memory alloy at the grain level is unavoidable due to the differences in the grain orientation and the grain morphology, which can be validated by the heterogeneous distribution of misorientation based on EBSD experiment and the heterogeneous distribution of various lattice rotation angles based on CPFEM simulation. As a result, CPFEM based on the realistic RVE plays a significant role in predicting inhomogeneous deformation of polycrystalline NiTi shape memory alloy in terms of grain scale.

ACKNOWLEDGMENT

REFERENCES

1. O. Benafan, R. Noebe, S. Padula, A. Garg, B. Clausen, R. Vaidyanathan, *et al. Int. J. Plasticity* **51**, 103 (2013).
2. A. Isalgue, C. Auguet, R. Grau, V. Torra, N. Cinca, and J. Fernandez, *J. Mater. Eng. Perform.* **24**, 3323 (2015).
3. Y. Liu, *Acta Mater.* **95**, 411 (2015).
4. E. Twohig, P. Tiernan, J. Butler, C. Dickinson, and S. Tofail, *Acta Mater.* **68**, 140 (2014).
5. H. M. Paranjape, S. Manchiraju, and P. M. Anderson, *Int. J. Plasticity* **80**, 1 (2016).
6. F. Weafer, Y. Guo, and M. Bruzzi, *J. Mech. Behav. Biomed.* **53**, 210 (2016).
7. L. Hu, S. Jiang, Y. Zhang, Y. Zhao, S. Liu, and C. Zhao, *Intermetallics* **70**, 45 (2016).
8. K. M. Armattoe, M. Haboussi, and T. B. Zineb, *Int. J. Solids Struct.* **51**, 1208 (2014).
9. S. Haroush, E. Priel, D. Moreno, A. Busiba, I. Silverman, Y. Gelbstein, *et al. Mater. Design* **83**, 75 (2015).
10. M. Ardeljan, I. J. Beyerlein, B. A. McWilliams, and M. Knezevic, *Int. J. Plasticity* **83**, 90 (2016).
11. L. Li, L. Shen, G. Proust, C. K. Moy, and G. Ranzi, *Mat. Sci. Eng. A* **579**, 41 (2013).
12. H. Sheikh, R. Ebrahimi, and E. Bagherpour, *Mater. Design* **109**, 289 (2016).
13. S. Manchiraju and P. M. Anderson, *Int. J. Plasticity* **26**, 1508 (2010).
14. L. Qiao and R. Radovitzky, *J. Mech. Phys. Solids.* **93**, 93 (2016).
15. C. Yu, G. Kang, and Q. Kan, *J. Mech. Phys. Solids.* **82**, 97 (2015).
16. R. Hill and J. Rice, *J. Mech. Phys. Solids.* **20**, 401 (1972).
17. Y. Huang, *A User-Material Subroutine Incorporating Single Crystal Plasticity in the ABAQUS Finite Element Program*, pp.1-21, Harvard University, USA (1991).
18. D. Peirce, R. Asaro, and A. Needleman, *Acta Metall.* **30**, 1087 (1982).
19. H. Abdolvand, M. R. Daymond, and C. Mareau, *Int. J. Plasticity* **27**, 1721 (2011).
20. S.-Y. Jiang, Y.-Q. Zhang, Y.-N. Zhao, M. Tang, and W.-L. Yi, *J. Cent. South Univ.* **20**, 24 (2013).
21. R. J. Asaro, *Adv. Appl. Mech.* **23**, 1 (1983).
22. L. Lv and L. Zhen, *Mat. Sci. Eng. A* **528**, 6673 (2011).
23. O. Diard, S. Leclercq, G. Rousselier, and G. Cailletaud, *Int. J. Plasticity* **21**, 691 (2005).
24. P. Van Houtte, L. Delannay, and S. Kalidindi, *Int. J. Plasticity* **18**, 359 (2002).
25. L.-T. Li, Y. Lin, L. Li, L.-M. Shen, and D.-X. Wen, *J. Mater. Eng. Perform.* **24**, 1294 (2015).
26. K.-S. Zhang, J. W. Ju, Z. Li, Y.-L. Bai, and W. Brocks, *Mech. Mater.* **85**, 16 (2015).
27. J. Segurado and J. Llorca, *Comp. Mater. Sci.* **76**, 3 (2013).
28. R. Quey, P. Dawson, and F. Barbe, *Comput. Method. Appl. M.* **200**, 1729 (2011).
29. T. Erinosho, D. Collins, A. Wilkinson, R. Todd, and F. Dunne, *Int. J. Plasticity* **83**, 1 (2016).
30. M.-G. Lee, J. Wang, and P. M. Anderson, *Mat. Sci. Eng. A* **463**, 263 (2007).
31. M. Knezevic, I. J. Beyerlein, M. L. Lovato, C. N. Tomé, A. W. Richards, and R. J. McCabe, *Int. J. Plasticity* **62**, 93 (2014).
32. J. Wert, Q. Liu, and N. Hansen, *Acta Mater.* **45**, 2565 (1997).